 doi:10.20944/preprints202012.0105.v1

Mapping built-up land with high accuracy using Fourier transformation and temporal correction

Jinzhu Wang [a,b,*], Michalis Hadjikakou [a], Brett A. Bryan [a]

[a] Centre for Integrative Ecology, School of Life and Environmental Sciences, Deakin University, VIC 3125, Melbourne, Australia

[b] Deakin-SWU Joint Research Centre on Big Data, Faculty of Science, Engineering and Built Environment, Deakin University, VIC 3125, Australia

Corresponding author: wangjinz@deakin.edu.au (J. Wang), Centre for Integrative Ecology, School of Life and Environmental Sciences, Deakin University, VIC 3125, Melbourne, Australia.

Highlights

- Mapping built-up land accurately is essential for urban policy and planning.
- We used Fourier transformation and temporal correction to map the North China Plain.
- Temporal predictors increased mapping accuracy from 85% to 93% in earlier years.
- Temporal correction increased accuracy further to >94%.
- High-accuracy mapping showed built-up land tripled from 1990 to 2019.

Abstract

Long-term, high-accuracy mapping of built-up land dynamics is essential for understanding urbanization and its consequences for the environment. Despite advances in remote sensing and classification algorithms, built-up land mapping using early satellite imagery (e.g., from the 2000s and earlier) remains prone to uncertainty. We mapped the extent of built-up land in

 doi:10.20944/preprints202012.0105.v1

the North China Plain, one of China's most important agricultural regions, from 1990 to 2019 at three-year intervals. Using dense time-stack Landsat data, we applied discrete Fourier transformation to create temporal predictors and reduce mapping uncertainties for early years. We improved overall accuracy by 8% compared to using spectral and indices predictors alone. We implemented a temporal correction algorithm to remove inconsistent pixel classifications, further improving accuracy to a consistently high level (>94%) across years. A cross-product comparison showed that our study achieved the highest levels of accuracy across years. Total built-up land in the North China Plain increased from 37,941 km^2 in 1990–1992 to 131,578 km^2 in 2017–2019. Consistent, high-accuracy built-up land mapping provides a reliable basis for policy planning in one of the most rapidly urbanizing regions of the planet.

Keywords: Built-up land; Fourier transformation; high-accuracy mapping; temporal correction.

 doi:10.20944/preprints202012.0105.v1

1. Introduction

Economic development and population growth have led to drastic changes of the Earth's terrestrial surface, not least through the expansion of built-up lands (Elmore et al., 2012), with urbanization continuing to accelerate in developing countries (United Nations, 2014). Built-up land is defined as land cover comprising more than 50% human-made structures such as roads, buildings, and agricultural and industrial facilities (Schneider and Mertes, 2014). Built-up land plays an essential role in material and energy cycling between humans and the environment, such as water and carbon cycling (Chen et al., 2020; Hou et al., 2020; Wang et al., 2018), pollution (Shrivastava et al., 2019; Yue et al., 2020), agricultural production (Brown, 1995), biodiversity conservation (Filazzola et al., 2019), ecosystem services (Bryan et al., 2018; Ye et al., 2018) and climate change, both at micro and macro levels (Lamb et al., 2019).

Accurately tracking the dynamics of built-up land is essential to linking human activities with ecological, environmental, and climatic impacts and supporting policy and planning for sustainable development (Vannier et al., 2019). Tracking built-up land dynamics with high accuracy over time is a significant challenge because mapping for earlier years (e.g., the 1990s) is often less accurate than for more recent times (e.g., 2010 onwards). For example, Landsat Operational Land Imager (OLI, with data available from 2013) showed higher classification accuracy than Landsat Thematic Mapper (TM, with data available from 1984 to 2011) when mapping urban areas in East Attica, Greece (Poursanidis et al., 2015). Inconsistencies can also arise when mapping through time, because bare soil has a similar spectral character to built-up land and is commonly misclassified (Gong et al., 2020; Li et al., 2015; Li and Gong, 2016). In addition, random noise such as cloud and cloud shadows can also lead to inconsistencies in the built-up land mapping (Foga et al., 2017). Unfavorable atmospheric conditions such as cloud cover can compromise satellite observation, hence built-

 doi:10.20944/preprints202012.0105.v1

up land mapping may require additional images from a broader temporal range (Liu et al., 2018). Increasing classification accuracy in earlier years, removing inconsistent classification, and using an appropriate time frame is therefore crucial for mapping built-up land with high accuracy through time.

Open-data policies combined with advances in computation facilities and innovative algorithms have enabled built-up land to be mapped at high resolution across larger extents, at greater frequency, and over longer periods than before (Li et al., 2016). Two strategies are typically used to increase mapping accuracy and reduce inconsistencies: 1) integrating multisource data and 2) using temporal consistency correction. For example, the Visible Infrared Imaging Radiometer Suite (VIIRS) nighttime light (NTL) has been used as a binary mask to exclude non-urban land (Gong et al., 2020; He et al., 2019; Liu et al., 2019). Sentinel-1 Synthetic Aperture Radar (SAR) data have been merged with Landsat data to increase classification accuracy (Gong et al., 2020; Zhang et al., 2020). The tendency of built-up land to not revert to nature or agriculture (i.e., its irreversibility) has also been used to correct inconsistent multi-temporal classifications (Li et al., 2015) and produce stable and reliable control points (Liu et al., 2019). However, the accuracy of built-up land mapping in earlier years is typically lower than that based on more recent remote-sensing data (e.g., after 2013), possibly due to the spectral confusion of early data (Poursanidis et al., 2015).

Spectral features and vegetation indices have been used to map built-up land, but temporal features such as land surface phenology have typically been overlooked (Jönsson et al., 2018). Generally, temporal features are derived from indices such as the normalized difference vegetation index (NDVI) using a smoothing method (Wang et al., 2017), such as a logistic model (Elmore et al., 2012), a Savitzky–Golay filter (Chen et al., 2004), quadratic functions (Beurs and Henebry, 2004), and Discrete Fourier Transform (Wang et al., 2019). Although temporal features have been coupled with change-detection methods to determine

 doi:10.20944/preprints202012.0105.v1

when other land types were converted to built-up land (Liu et al., 2019), they have been infrequently adopted as mapping predictors (Zeng et al., 2020). Because temporal features capture relatively stable greenness patterns following interannual plant growth cycles, we hypothesize that they could also mitigate the spectral confusion of earlier satellite data and increase the accuracy of built-up land mapping.

This study aims to accurately track built-up land dynamics at three-year intervals from 1990 to 2019 using dense-stack Landsat data and temporal correction. The North China Plain region was chosen as the study area because of the fierce competition between urbanization and farmland over land resources (Jin et al., 2019). First, we used the Discrete Fourier Transformation to derive temporal features based on dense-stack indices of Landsat data (Odenweller and Johnson, 1984; Song et al., 2016). Second, we tested the performance of different predictors by adding those sequentially to the classification. A temporal correction algorithm was then deployed to remove inconsistent pixel classifications. Finally, we conducted a cross-product comparison to assess our results against other datasets (Stehman and Foody, 2019). Long-term, high-resolution, and high-frequency built-up land maps with high accuracy can be used as reliable inputs to understand regional urban development and link social-economic change to environmental impacts.

2. Methods

The approach taken in this study is summarized in Figure 1. Due to its high computational performance and vast historical satellite imagery, Google Earth Engine was used to process all remotely sensed data and map built-up land (Gorelick et al., 2017). Control points were visually checked using Landsat images from 1990–1992 and Google Earth high-definition images (from GeoEye, WorldView, SPOT, and the Pleiades) from 2014 and 2019. We randomly held out 25% of the control points as validation samples. Cloud-free images,

Preprints (www.preprints.org) | NOT PEER-REVIEWED | Posted: 4 December 2020 doi:10.20944/preprints202012.0105.v1

indices images, temporal features, terrain, and meteorology data were sequentially added to a Random Forest (RF) classifier. A temporal correction algorithm was then applied to remove inconsistent classifications. Lastly, a cross-product comparison was carried out using the hold-out samples.

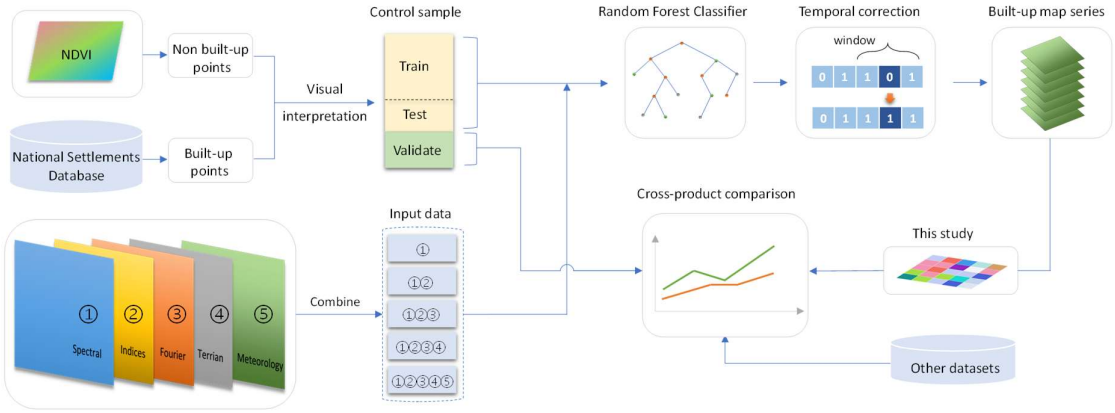

Figure 1. Flowchart outlining the methods used to map built-up land in the North China Plain. The National Settlements Database stores the geo-coordinates of government departments and state-owned companies from 2000 (http://www.resdc.cn/). The spectral data refer to the cloud-free image produced from the Landsat image. Indices variables refer to the normalized difference vegetation index (NDVI), enhanced vegetation index (EVI), and normalized difference built-up index (NDBI). The Fourier data are coefficients derived from a discrete Fourier transformation of indices image. Terrain data were derived from the digital elevation model and slope from the Shuttle Radar Topography Mission. Meteorology data were taken from the China Meteorological Forcing Dataset (http://data.tpdc.ac.cn/).

2.1 Study area

Five middle and eastern provinces of China corresponding to the North China Plain region were selected as the study area (Figure 2). The area spanned 780,000 km^2 and five provinces (i.e., Henan, Hebei, Shandong, Anhui, and Jiangsu) and two municipalities (Beijing and Tianjin). The study area is one of China's fastest developing regions, with the urban

Preprints (www.preprints.org) | NOT PEER-REVIEWED | Posted: 4 December 2020 doi:10.20944/preprints202012.0105.v1

population rate (excluding the two metropoles) tripling from ~20% in 1990 to ~60% in 2018 (National Bureau of Statistics of China, 2019b). The North China Plain holds a strategic position in China in terms of economic development and food security (Song and Deng, 2015), generating ~37% of the gross domestic product and ~35% of China's grain production in 2019 (National Bureau of Statistics of China, 2019a, 2019b). The tension between rapid economic development and food production in the study area therefore calls for accurate quantification of built-up land dynamics to support policy formulation and decision making (Li et al., 2020; Liu et al., 2020).

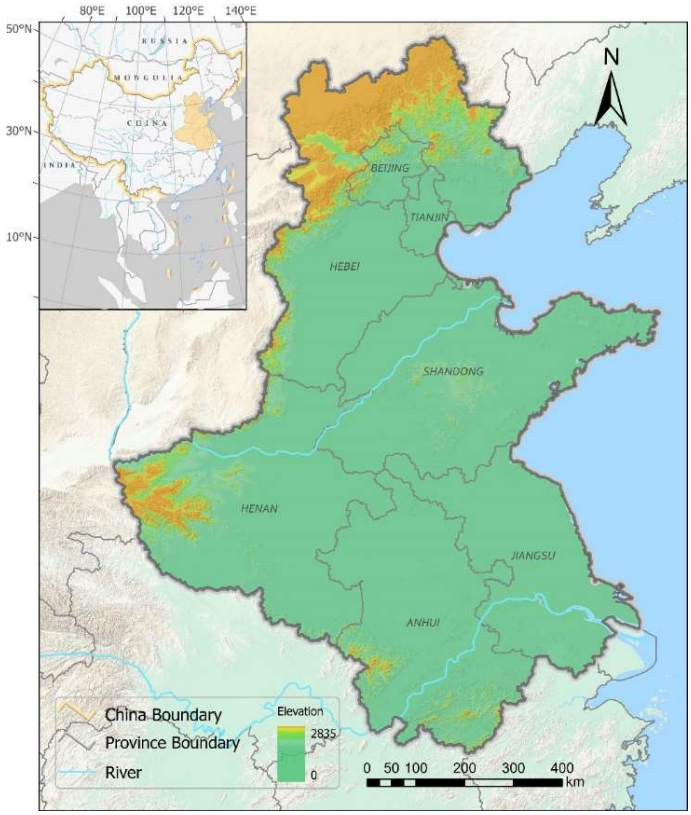

Figure 2. Map of the North China Plain. The study area is one of China's food basins and is dominated by vast cultivated lands.

Preprints (www.preprints.org) | NOT PEER-REVIEWED | Posted: 4 December 2020 doi:10.20944/preprints202012.0105.v1

2.2 Data and input predictors

We used five types of remotely sensed data as predictors to map built-up areas (

Table **1**). Spectral predictors comprised cloud-free images computed from Landsat and Sentinel 2A. Indices predictors comprised the NDVI, enhanced vegetation index (EVI), and normalized difference built-up index (NDBI) computed from Landsat cloud-free data. The Fourier predictors were the coefficients derived from the Discrete Fourier Transformation of dense time stacks of indices images. Lastly, meteorology data were taken from the China Meteorological Forcing Dataset (He et al., 2020) and terrain data were taken from the Shuttle Radar Topography Mission.

Table 1. Input predictors for built-up land mapping. TM: Thematic Mapper, ETM+: Enhanced Thematic Mapper Plus, OLI: Operational Land Imager, MSI: Multispectral Instrument, NDVI: normalized difference vegetation index, EVI: enhanced vegetation index, and NDBI: normalized difference built-up index. The resolution of the panchromatic band of Landsat ETM+ and OLI is 15 m. The resolution of B1, B9, and B10 of Sentinel 2 MSI is 60 m, and that of B5-7, B8A, B11, and B12 is 20 m.

Input type	Source	Spatial resolution	Number of bands	Years
Spectral	Landsat TM	30 m	7	1990-2010
	Landsat ETM+	30 m	9	2011-2013
	Landsat OLI	30 m	11	2014-2019
	Sentinel-2A MSI	10 m	13	2015-2019
Indices	NDVI	30 m	1	1990-2019
	EVI	30 m	1	1990-2019
	NDBI	30 m	1	1990-2019
Fourier	Coefficients of the Discrete Fourier Transformation	30 m	24	1990-2019
Meteorology	China Meteorological Forcing Data	1°	7	1990-2019
Terrain	Elevation	30 m	1	1990-2019
	Slope	30 m	1	1990-2019

The spectral predictors were cloud-free images produced from Landsat and Sentinel-

Preprints (www.preprints.org) | NOT PEER-REVIEWED | Posted: 4 December 2020 doi:10.20944/preprints202012.0105.v1

2A, the detailed data information can be seen in the supplementary information 1.1 (SI-1.1). Cloud-free Landsat images were produced using the *ee.Algorithms.Landsat.simpleComposite* module in the Google Earth Engine platform. For each pixel in the collection of Landsat images, this module computed a cloud score (0–100) and derived the median value from pixels with a cloud score <10 to create a cloud-free image. For the cloud-free image of Sentinel 2 MSI, the Quality Assessment band, indicating whether the pixel was covered by cloud and cirrus, was used to remove cloudy pixels. After removing cloudy pixels, the median value of the remaining pixels was mosaicked to create a cloud-free image.

NDVI, EVI, and NDBI were selected as indices predictors because NDVI and EVI are robust for delineating land covers (Li et al., 2015), and NDBI suits the purpose of built-up mapping (Li and Chen, 2018). We calculated these indices as follows:

$$NDVI = (NIR - R) / (NIR + R) \quad (1)$$

$$EVI = 2.5 \times ((NIR - R) / (NIR + 6 \times R - 7.5 \times B + 1)) \quad (2)$$

$$NDBI = (SWIR1 + NIR) / (SWIR1 - NIR) \quad (3)$$

where NIR refers to the near-infrared band, R refers to the red band, B refers to the blue band, and SWIR1 refers to the first shortwave infrared band.

The Discrete Fourier Transformation approximates a series of discrete values by summing up a linear function and several pairs of sinuate functions. The fitting formulation was as follows:

$$p_t = \beta_0 + \beta_1 t + \sum_{k=1}^{n} [\alpha_k \cos(2\pi k \omega t) + \theta_k \sin(2\pi k \omega t)] + e_t \quad (4)$$

where t is the time difference in year fractions compared to 1970, p_t is the pixel value at time t, n is the number of sinuate function pairs, β_0 and β_1 are the coefficients of the linear function, α_k and θ_k are the sinuate coefficients, ω is the frequency, and e_t is the error between the actual observation and the fitted value.

In practice, n and data volume should be determined before fitting. We chose $n = 3$ and

Preprints (www.preprints.org) | NOT PEER-REVIEWED | Posted: 4 December 2020 doi:10.20944/preprints202012.0105.v1

used three years of normalized indices data for the transformation to minimize the sum of mean-squared error and avoid overfitting (SI-1.2). Meanwhile, we selected $\omega = 1$ based on the life cycle frequency of most of the vegetation in the study area (Tang et al., 2020). The Discrete Fourier Transformation was applied to fit the normalized indices to generate temporal predictors (Figure 3). Eight coefficients were generated per index, and a total of 24 coefficient bands were created as temporal predictors.

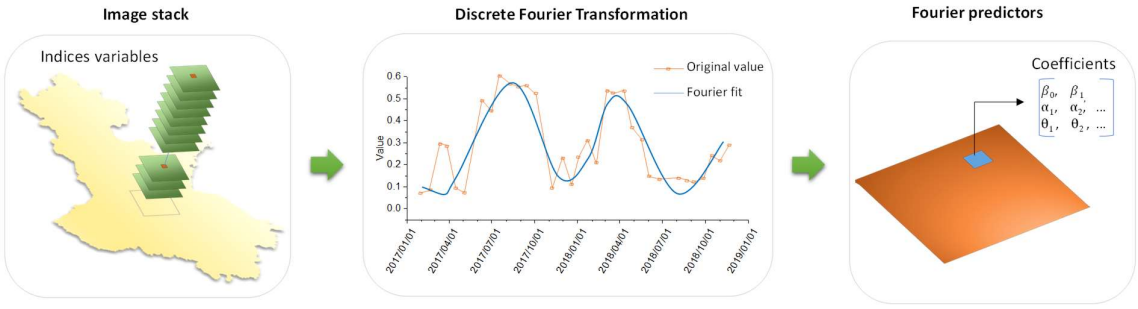

Figure 3. The Discrete Fourier Transformation on indices data. Indices data were stacked and the coefficients of the fitting function were derived as Fourier predictors.

The China Meteorological Forcing Dataset (http://data.tpdc.ac.cn/) and Shuttle Radar Topography Mission data were incorporated as additional predictors to reduce interference by different climate and terrain conditions. The China Meteorological Forcing Dataset includes seven variables: temperature (K), air pressure (Pa), specific humidity (kg kg^{-1}), wind speed (m s^{-1}), downward shortwave radiation (W m^{-2}), downward longwave radiation (W m^{-2}), and precipitation (mm yr^{-1}). The Shuttle Radar Topography Mission data used in this study included elevation and slope.

2.3 Built-up land mapping

2.3.1 Control point collection

Control points were collected with visual interpretation (SI-2). Built-up and non-built-

 doi:10.20944/preprints202012.0105.v1

up control points were collected separately. Raw built-up points were taken from the National Settlements Database of China (http://www.resdc.cn/). Raw non-built-up points were generated via stratified sampling using NDVI. Following visual interpretation, a total of 8,000 control points were collected, with an equal number of built-up and non-built-up points (i.e., 4,000) to reduce bias caused by uneven sample distribution (Stehman and Foody, 2019). A sensitivity test showed that using ~50% of control samples was sufficient to achieve high-accuracy mapping (SI-3.1). Therefore, ~75% of control samples were used as the training sample for mapping (among them, 70% were used in classification and 30% to calculate accuracy), while the remaining ~25% were held out as validation samples for the cross-product comparison.

2.3.2 Classifying built-up land

Random Forest (RF) is an ensemble learning algorithm that was selected for classification due to its flexibility in capturing non-linear patterns between independent and dependent variables (Calderón-Loor et al.). The tree-based structure of RF is also efficient in classifying high-dimensional data (Wang et al., 2019). To grow trees for the RF, we set the split nodes as the square root of the number of input predictors, the bag fraction to 50%, and the minimum leaf nodes to 1. The number of trees in the RF was set to 100 because no more improvements could be achieved by further increasing tree number (SI-3.1). In the mapping process, built-up land pixels were allocated a value of 1 and non-built-up land pixels a value of 0.

Predictors were sequentially added to the classification in the following order: spectrum, indices, Fourier, terrain, and meteorology predictors. Traditional classification typically uses spectral and indices predictors, so we first mapped built-up land using those. The Fourier predictors were then incorporated to test classification improvement with temporal features. Lastly, terrain and meteorology data were added to reduce interference by climate and terrain

Preprints (www.preprints.org) | NOT PEER-REVIEWED | Posted: 4 December 2020 doi:10.20944/preprints202012.0105.v1

conditions.

All five types of predictors were used in mapping. We classified built-up land 10 times, each time using a different sample of random control points. In each classification, 70% of the training samples were randomly selected to train the RF classifier, and the remaining 30% were used to compute overall accuracy. Uncertainty was then calculated as the standard error of the accuracies of the 10 simulations. To derive the final classification of built-up land, we summed the 10 classifications and identified the pixels classified as built-up land more than 4 out of 10 times. Four was chosen as the threshold as it led to the highest classification accuracy (SI-3.2).

Based on the typical irreversibility of built-up land development and expansion (Gong et al., 2020; Li et al., 2015), we constructed temporal check rules to correct inconsistent pixel classifications over time (Figure 4). Built-up land extent in earlier years could not exceed the built-up land extent mapped in later years. For each built-up land map, n subsequent classifications were summed to construct a built-up extent, and pixels of $>n/2$ value in the built-up extent were selected to produce a mask to update the original classification according to a "majority vote" rule (Li et al., 2015). In this study, we set $n = 2$ by balancing the amount of data used as a mask and resulting improvements in accuracy (SI-4). This temporal correction process was iterated eight times to remove inconsistencies.

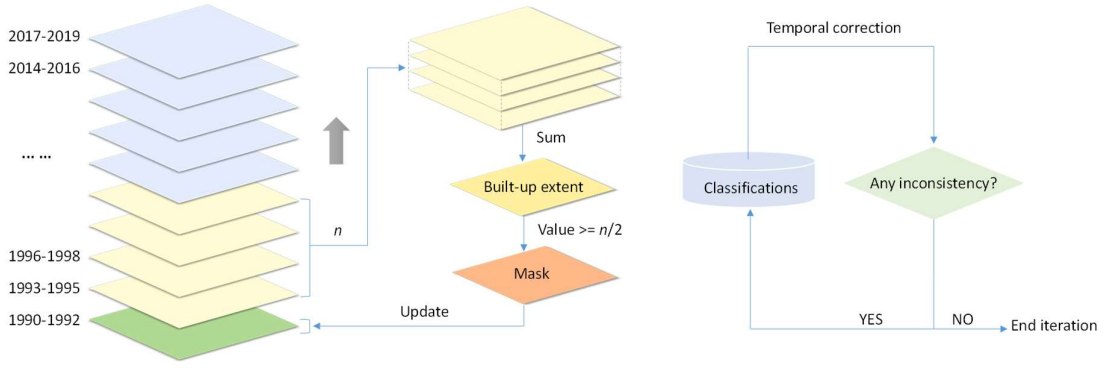

Figure 4. Temporal correction for built-up land mapping. Left, temporal correction process for each iteration; right, the stop condition of the iteration. Here we choose $n = 2$ based on a

Preprints (www.preprints.org) | NOT PEER-REVIEWED | Posted: 4 December 2020 doi:10.20944/preprints202012.0105.v1

sensitivity test (SI-4.1).

2.3.3 Cross-product comparison

We compared our data to other datasets targeting a similar land cover (such as impervious surfaces and human settlements) or including an urban/built-up land layer (Table 2). Built-up area and overall accuracy were used for the comparison. The validation sample (25% of all control samples) was used to compute overall accuracy because it was not used in the original classification of this study, thereby ensuring a reliable comparison (Stehman and Foody, 2019).

Table 2. Global built-up land datasets used for comparison with the outputs of this study. GAIA: Global Artificial Impervious Area, ESA CCI: European Space Agency Climate Change Initiative, GHSL: Global Human Settlement Layer, MCD12Q1: MODIS Land Cover Type Product, MERIS: Medium-spectral Resolution Imaging Spectrometer, SPOT-VGT: Strategic Planning Online Tool Vegetation Instrument, PROBA-V: Project for On-Board Autonomy Vegetation, AVHRR: Advanced Very High-Resolution Radiometer, and MODIS: Moderate Resolution Imaging Spectroradiometer.

Dataset	Sensors	Resolution	Timeframe	Source
GAIA	Landsat TM/ETM+/OLI, Sentinel-1&2, VIIRS NTL	30 m	Annual map 1985–2018	Gong et al., 2020
ESA CCI	MERIS, SPOT-VGT, PROBA-V AVHRR	300 m	Annual map 1992–2015	ESA, 2017
GHSL	Landsat TM/ETM+/OLI	38 m	1975, 1990, 2000, 2014	Pesaresi et al., 2015
Global Urban Dynamics	Landsat, VIIRS NTL	30 m	1990, 1995, 2000, 2005, 2010, 2015	Liu et al., 2018
Global Urban Expansion	VIIRS NTL, MODIS	1000 m	1992, 1996, 2000, 2006, 2010, 2016	He et al., 2019
MCD12Q1	MODIS	500 m	Annual map 2001–2019	Sulla-Menashe and Friedl, 2018
Global Impervious Surface	Landsat, Sentinel	30 m	2015	Zhang et al., 2020
GlobeLand30	Landsat TM/ETM+/OLI, Gaofen-1	30 m	2000, 2010, 2020	Jun et al., 2014

Preprints (www.preprints.org) | NOT PEER-REVIEWED | Posted: 4 December 2020 doi:10.20944/preprints202012.0105.v1

3. Results

3.1 Built-up land mapping using different predictors

The performance of different predictors is shown in Figure 5. For spectral predictors, the Sentinel-2A MSI data was the most robust predictor, increasing classification accuracy from ~83% in 2011–2013 to ~93% in 2017–2019. The next best predictors were the Fourier and indices predictors: the addition of indices data brought a 3% gain in accuracy and Fourier predictors brought an additional 8% gain. For classifications in the 1990s and 2000s, incorporating the Fourier predictors raised the overall accuracy to ~92%, similar to the overall accuracy in 2014–2019 using Sentinel-2A MSI data. Hence, incorporating temporal predictors in early years (Landsat 5 TM or Landsat 7 ETM+) enabled the mapping of built-up land with an accuracy similar to the classification based on data sourced from more advanced recent sensors (i.e., Landsat 8 OLI and Sentinel-2A MSI).

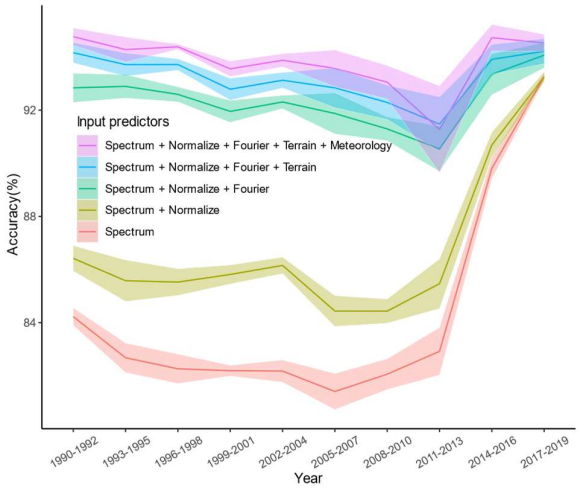

Figure 5. Accuracy of different predictors when mapping built-up land. Lines show the median value of 10 classifications with different sample splits; the margins show the standard error.

Built-up land mapping in 1990–1992 was selected to explore the spatial performance of spectral, indices, and Fourier predictors (Figure 6). Region 1 (row 1, Figure 6) shows villages

 doi:10.20944/preprints202012.0105.v1

surrounded by farmland, where the classification using spectral predictors misclassified as built-up land large areas of farmland near villages. Adding indices predictors to spectral predictors reduced the misclassification of farmland to built-up land, but some misclassifications near villages remained. Incorporating Fourier predictors removed nearly all misclassified farmland, delineating the built-up land clearly. Region 2 (row 2, Figure 6) shows a town surrounded by bare lands. The classification using spectral predictors misclassified most bare land to build-up land, and indices predictors worsened the classification. After incorporating Fourier predictors, the town was clearly distinguished from bare lands. Regions 3 and 4 (rows 3 and 4, Figure 6) were located in more humid areas than regions 1 and 2, and the incorporation of Fourier predictors removed weather interference and provided more accurate mapping. Figure 6 shows that bare lands and farmland rotation are primary confounding factors for built-up land mapping. The addition of indices predictors removed misclassifications in Regions 1 and 3 but worsened classification in regions 2 and 4. However, the Fourier predictors provided stable delineation for built-up land mapping across the four example regions.

Preprints (www.preprints.org) | NOT PEER-REVIEWED | Posted: 4 December 2020 doi:10.20944/preprints202012.0105.v1

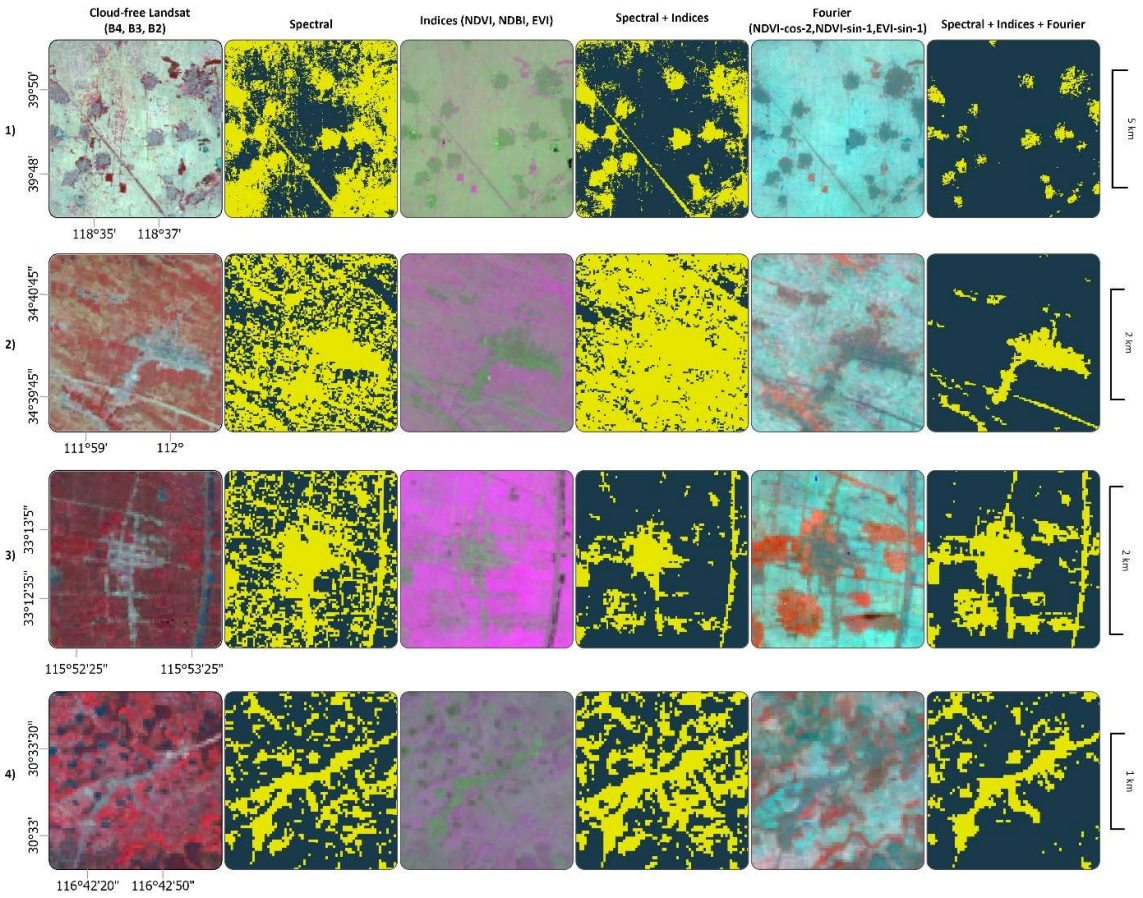

Figure 6. Spatial improvement in built-up land mapping for four exemplar regions. We used a false-color composition scheme to display predictors and a two-color map to represent the classification results (with yellow indicating built-up land and gray other land classes). Regions 1 and 2 were located in the northern, temperate area; regions 3 and 4 were located in the more humid southern study area. NDVI-cos-2: second frequency coefficient band of the discrete Fourier transformation on NDVI.

3.2 Accuracy improvements via temporal correction

Figure 7a shows classification accuracy before and after temporal correction. Temporal correction successfully increased built-up classification accuracy to consistently high levels. The highest accuracy increase (1.5%–2.5%) occurred in the last two periods, while the accuracy of the first two periods decreased by 0.1%–0.5%. We further inspected spatial improvements in 2011–2013 because the classification in this period had the lowest original

Preprints (www.preprints.org) | NOT PEER-REVIEWED | Posted: 4 December 2020 doi:10.20944/preprints202012.0105.v1

accuracy (Figure 7b). The Scan-Line Corrector failure of Landsat ETM+ produced inconsistent strips, which were accounted for by the temporal correction (regions A and C). Greenhouses (hazy and light gray patches in region B) were correctly removed by the temporal correction. Finally, the temporal correction also improved classification quality in hilly and barren areas (region D).

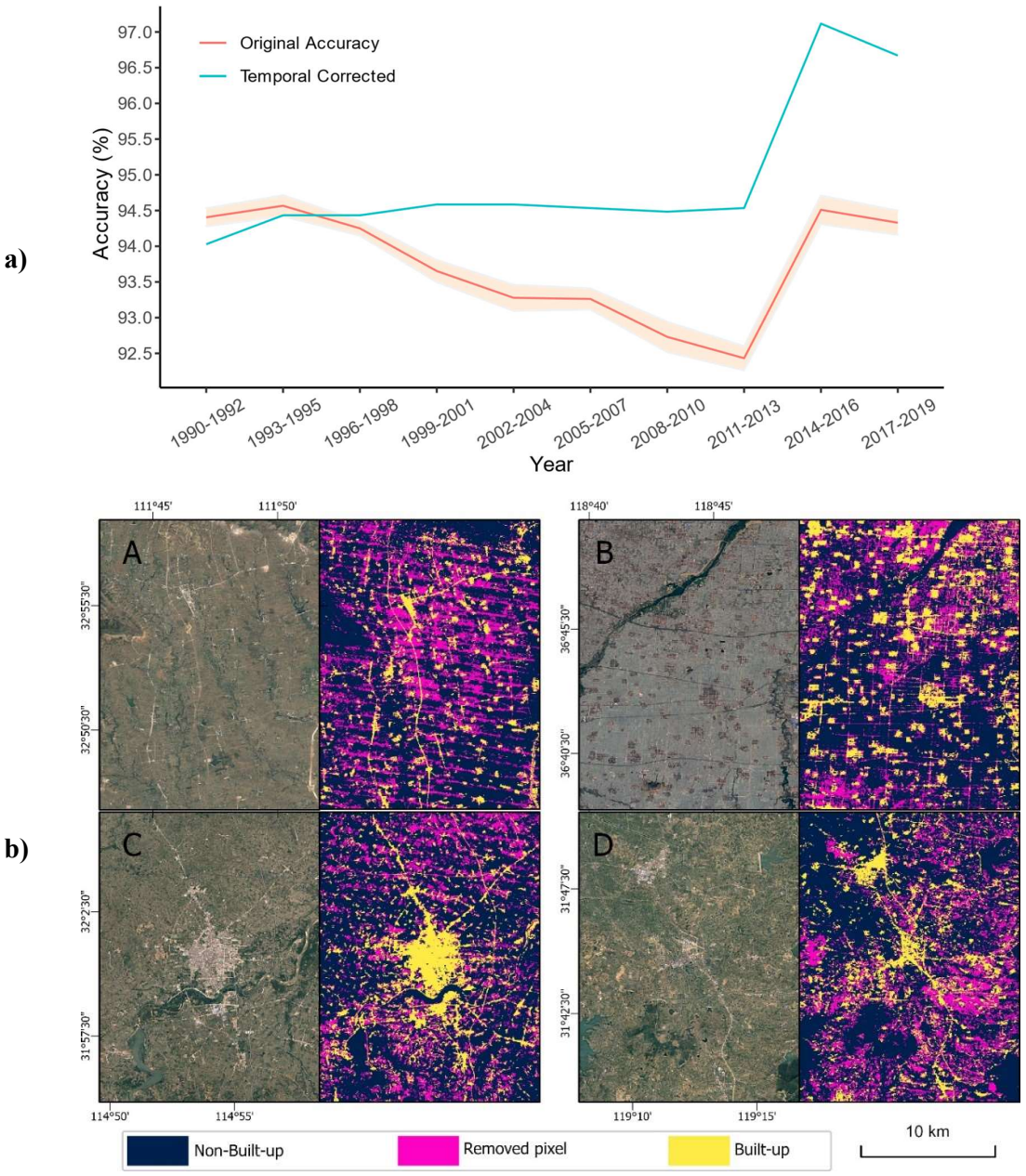

Figure 7. Improvement in overall accuracy and spatial performance when using temporal correction. True-color maps in b) were obtained from high-definition Google Earth images

 doi:10.20944/preprints202012.0105.v1

from December 2013.

3.3 Spatial-temporal change of built-up land

We mosaicked all temporally corrected classifications into one image and used a warm-cool color scheme to represent time from 1990 to 2019 (Figure 8). Cities in flat regions (e.g., Baoding, Shangqiu, and Changzhou) expanded radially outward. Cities near rivers (e.g., Xuyi and Xinyang) expanded against those, and cities in mountainous areas (e.g., Fengning) expanded along valleys.

Preprints (www.preprints.org) | NOT PEER-REVIEWED | Posted: 4 December 2020 doi:10.20944/preprints202012.0105.v1

Figure 8. Dynamic map of built-up areas from 1990 to 2019. Warm colors indicate earlier dates while cool colors indicate later dates. Hexagonal insets show zoomed-in views of selected cities.

Preprints (www.preprints.org) | NOT PEER-REVIEWED | Posted: 4 December 2020 doi:10.20944/preprints202012.0105.v1

The increase in built-up area accelerated over the study period, with all provinces tripling their built-up area (Figure 9). Across years, Shandong and Henan provinces had the first and second-largest built-up areas. Jiangsu province rose from the fifth-largest built-up land area to the third after 2004, while Hebei and Anhui had similarly low levels of built-up land area. Beijing and Tianjin showed similar amounts of built-up area for all periods and both increased rapidly.

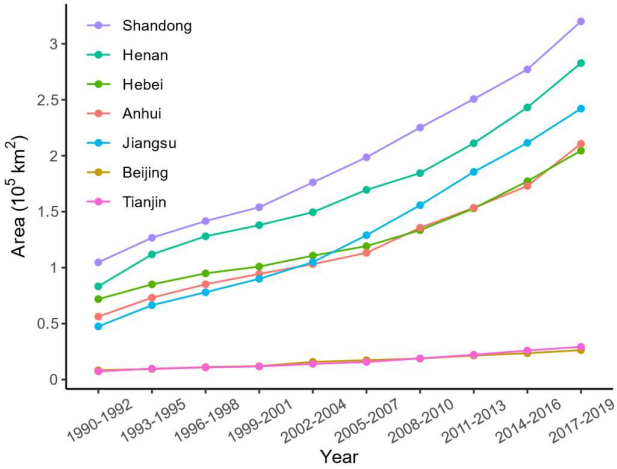

Figure 9. Change in built-up area in seven provinces of the North China Plain from 1990 to 2019.

3.4 Cross-product comparison

For the spatial comparison, we selected four cities that were evenly distributed across the study area and with datasets with three or more epochs (Figure 10). The low-resolution datasets (ESACCI, Global Urban Expansion, and MCD12Q1) missed many built-up lands in smaller villages and towns. The Global Urban Dynamics used high-resolution images of Landsat as input data, but the binary mask generated from the VIIRS NTL missed out-of-boundary built-up land. However, our data and the GAIA product captured built-up land in large cities and smaller villages and towns.

Preprints (www.preprints.org) | NOT PEER-REVIEWED | Posted: 4 December 2020 doi:10.20944/preprints202012.0105.v1

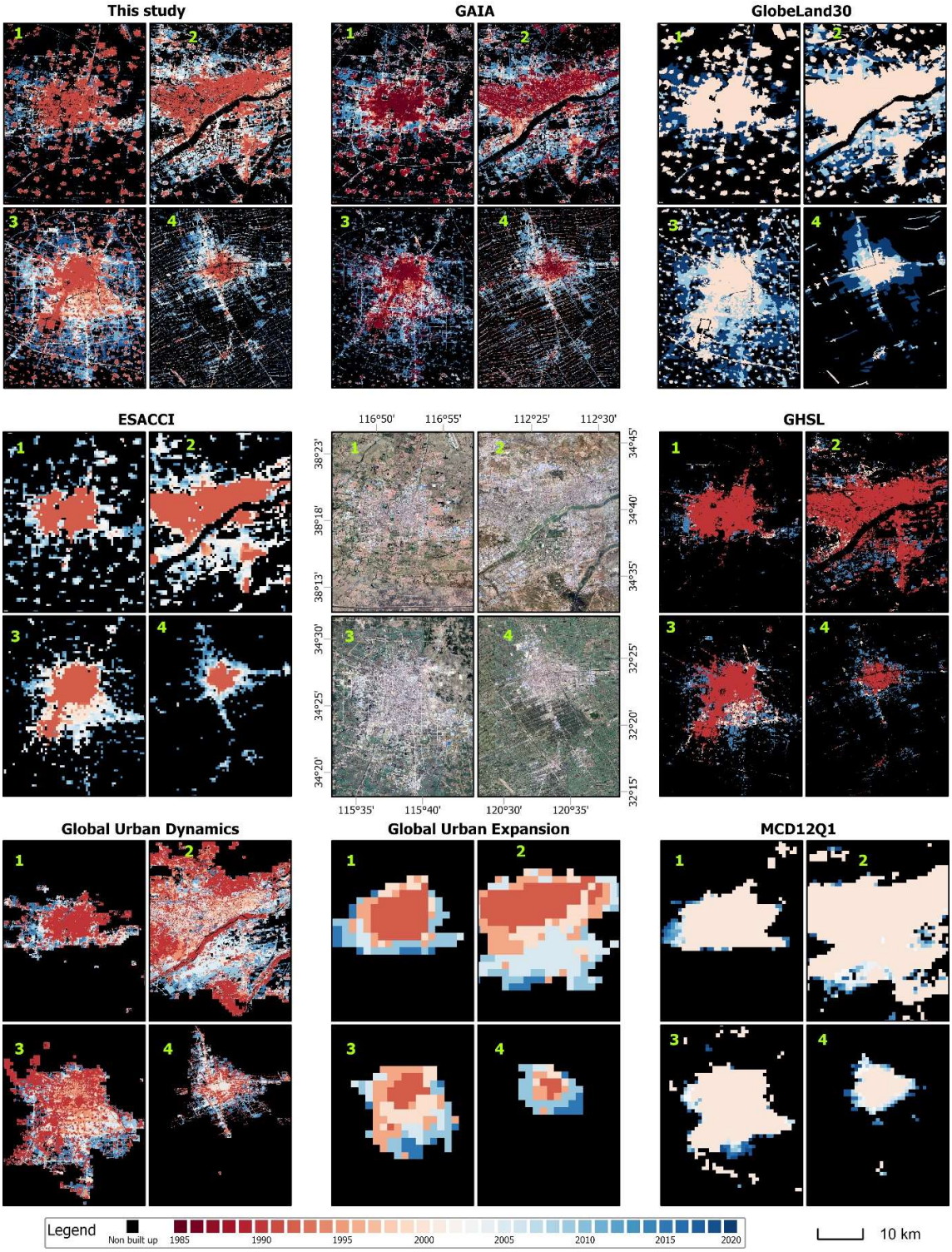

Figure 10. Dynamics of built-up area in four selected cities (1990–2019). The true color maps were taken from Google Earth high-definition images from 2019. GAIA: Global Artificial Impervious Area, ESA CCI: European Space Agency Climate Change Initiative, GHSL: Global Human Settlement Layer, MCD12Q1: MODIS Land Cover Type Product.

Preprints (www.preprints.org) | NOT PEER-REVIEWED | Posted: 4 December 2020 doi:10.20944/preprints202012.0105.v1

We further compared built-up areas and overall accuracy between our study and other datasets (Figure 11a). Our study computed the second largest built-up area throughout the study period, similar to other high-resolution datasets (i.e., GAIA, GHSL, and GlobeLand30). In the 1990s, our data were in agreement with GAIA and GHSL, while the ESACCI, Global Urban Dynamics, and Global Urban Expansion estimates were significantly lower than ours. GAIA, ESACCI, and our data showed rapid increases in built-up area, while GHSL, MODIS, Global Urban Dynamics, and the Global Urban Expansion showed linear increasing trends.

Due to their similar spatial resolution and land-cover definition, GAIA, Global Impervious Surface, and GlobeLand30 were selected for accuracy comparisons. The accuracy of our study was higher than GHSL and Global Impervious Surface by 10%, and 10-19% higher than GAIA, especially in earlier years. Our accuracy was consistently >94% across years, while that of the Global Impervious Surface and GlobeLand30 were ~85%, and GAIA's accuracy ranged from 75% in 1990 to 84% in 2017.

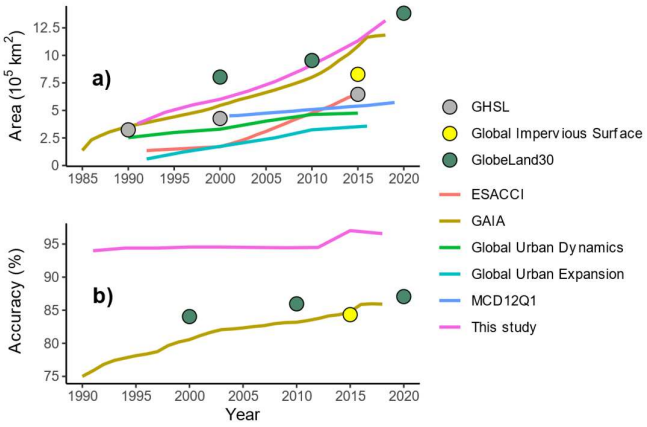

Figure 11. Area and overall accuracy comparison. The middle year of each period in this study was selected as the x-axis value (for example, 1991 was used to indicate the built-up area of 1990-1992).

 doi:10.20944/preprints202012.0105.v1

4. Discussion

Landsat has a long and continuous archive, which offers a unique opportunity for global and regional land observation (Deng and Zhu, 2020). However, lower quality data in earlier years can lead to poor performance in built-up land mapping and higher uncertainty in earlier points of time series (Gong et al., 2020; Poursanidis et al., 2015) . In this study, we used coefficients from a Discrete Fourier Transformation as temporal predictors and derived an 8% accuracy gain compared to using spectral and indices predictors only. Employing the temporal variables increased mapping accuracy for earlier years, even when using lower quality data (Landsat 5 TM or Landsat 7 ETM+), rivaling the mapping accuracy of more recent, higher-quality sensor data (Landsat 8 OLI and Sentinel MSI data). Bare land and farmland were commonly misclassified as built-up land using spectral and indices predictors only (Gong et al., 2019; Liu et al., 2018), but these errors were largely removed following the inclusion of temporal predictors. Our results captured finer-scale built-up features, such as buildings in small villages and towns, rather than solely focusing on large cities. As a result of higher accuracy, our study computed higher estimates of built-up areas than other datasets, except for GlobeLand30.

The effectiveness of Fourier predictors in delineating built-up lands is possibly because features captured in dense time stacks of remotely sensed data are less affected by random noise (e.g., cloud, cloud shadow, and seasonal changes in land surface) than snapshot spectral or indices images. Crop phenology and farming rotations lead to a regular greenness pattern in cultivated sites over the annual growing cycle, which is distinct from that of built-up lands (Zeng et al., 2020). Temporal predictors were sensitive to this distinction between built-up land and farmland. Similarly, it is difficult for spectral predictors and normalized indices to separate fallow lands from built-up lands, leading to uncertainties in mapping. Incorporating temporal predictors reduces this confusion and substantially increases the accuracy of built-up land

 doi:10.20944/preprints202012.0105.v1

mapping.

In addition to incorporating temporal predictors, we also implemented temporal correction to account for the general feature of irreversibility in built-up lands (i.e., once an area is converted to urban land, it tends to remain as urban land use (Li et al., 2015; Li et al., 2018);. We implemented the rule that built-up land in earlier years was unlikely to occur beyond the extent of built-up land in later years, thereby developing a temporal correction algorithm to remove incorrect pixel classifications. For example, our algorithm removed the misclassified strips caused by the ETM+ Scan-Line Corrector failure. Our method can be deployed on the Google Earth Engine platform and is more straightforward than other temporal correction algorithms. For example, Li et al. (2015) combined a majority vote rule and temporal reasoning to construct a spatial-temporal check algorithm, which required a complicated process to combine transition probabilities and neighborhood characteristics. In this study, we used built-up land maps of future years to iteratively mask out erroneous classified pixels in previous years, which was more straightforward to implement.

As a result of using temporal predictors and temporal correction, we achieved consistently high accuracy in built-up land mapping over a time series spanning 30 years. High uncertainty in built-up land mapping in the 1990s and 2000s has been reported in previous studies (Gong et al., 2020), and GAIA and GlobeLand30 showed lower performance in these years (Figure 11). Overall accuracy in this study was high and consistent across years (>94%).

The high quality of the data in this study addresses some of the challenges in understanding built-up land development and reduces uncertainties involved in quantifying land-use change induced environmental impacts (Dong et al., 2015). Built-up land occupies only a small portion of the global terrestrial surface but hosts more than half of the world's population (Chen et al., 2020). Indeed, 70% of global anthropogenic greenhouse gas emissions in 2016 and 80% of local natural habitat loss in 2018 have been linked to the development of

 doi:10.20944/preprints202012.0105.v1

built-up lands (Hopkins et al., 2016; Ke et al., 2018). Therefore, an accurate understanding of the dynamics of built-up land over time is critical to addressing the social and environmental challenges that threaten a sustainable future in rapidly urbanizing areas, including our study area.

Our consistent, high-accuracy data product could be used in urban policy and planning. For example, urban growth models based on cellular automata use historical data to project future scenarios, but errors in historical data can propagate throughout the projection, reducing confidence in the results (Clarke and Johnson, 2020). This study provides reliable historical data that enables built-up area development to be projected with high confidence. Environmental change can also be quantified more precisely using accurate built-up land maps. For example, the Integrated Valuation of Ecosystem Services and Trade-offs (InVEST) model uses land-use maps as a proxy to calculate carbon sequestration, water yield, crop production, and habitat quality (Tallis et al., 2011). High-quality built-up land mapping data can provide more reliable input variables to calculate the anthropogenic impacts of urbanization.

Spatially explicit policies and planning are essential for supporting sustainable development, and one requirement for formulating such policies is access to high-quality data. The study area is unique in China for its strategic position, rapid urbanization, and essential agricultural productivity (Song and Deng, 2015). To boost the economy of the study area, the Chinese government has announced a series of development plans, such as the Beijing-Tianjin-Hebei Urban Agglomeration development plan (Fang et al., 2019) and the Central Plains City Group development plan (Li et al., 2020). These plans include mega-infrastructure projects (e.g., high-speed railways and long-distance expressways) to enhance economic flow among cities (Li et al., 2020). In parallel, to safeguard food security, the Chinese government has also enacted strict farmland protection regulations (e.g., the Basic Farmland Protection Regulations) that prohibit farmland from being converted to built-up lands (Liu et al., 2020). Therefore, an

 doi:10.20944/preprints202012.0105.v1

accurate understanding of built-up land dynamics is critical to formulating effective development plans that balance rapid urbanization with increased demand for food production (Zhong et al., 2020). Accurate historical built-up data can be used to project future economic development, as well as derive opportunity costs for future urban expansion (e.g., in terms of reduced food security). As a result, urbanization, food security, and sustainability can be coordinated under one framework, promoting the formulation of spatially explicit policies and regulations.

Our study suffers from several limitations and uncertainties. We derived temporal features from the Discrete Fourier Transformation based on three years of indices images. Hence the exact date of built-up land development cannot be determined at a finer resolution than three years. Another uncertainty was introduced by the temporal correction methodology, which assumes that built-up land in 1990–1992 remained unchanged during the study period. Small areas of built-up land could have been converted to other land types over time (Fu et al., 2019). However, such conversions typically only comprise a small portion of the total built-up land area (Gong et al., 2020).

5. Conclusion

In this study, we incorporated temporal features based on a dense time stack of Landsat imagery and a temporal correction method to map the spatial extent of built-up land in the North China Plain (1990–2019). Incorporating temporal predictors increased overall accuracy by 8% compared to using spectral and indices predictors alone. The temporal correction successfully removed incorrectly classified pixels and increased overall accuracy in all periods to a consistently high level (>94%). All provinces and cities in the study region tripled their built-up area over the last three decades, revealing fierce competition between urban and agricultural land uses. Consistent, high-accuracy and long time-series of built-up land data can

 doi:10.20944/preprints202012.0105.v1

be used to understand recent patterns of rapid urbanization, quantify impacts for food security and the environment, model future land-use change, and inform policy and planning for managing future urbanization and sustainable development.

Author responsibilities

J.W, B.A.B, and M.H designed the analysis. J.W analyzed the data and drafted the initial version of this paper. B.A.B contributed to the design of control points, data visualization, and interpretation, and writing. M. H contributed to the interpretation of the results.

Funding

This research was funded by a Deakin University Postgraduate Research Scholarship.

Declaration of Competing Interest

None

Acknowledgments

The control points were visually interpreted by Lauren McManus.

 doi:10.20944/preprints202012.0105.v1

References

Beurs, K.M. de, Henebry, G.M. 2004. Land surface phenology, climatic variation, and institutional change: analyzing agricultural land cover change in Kazakhstan. *Remote Sens. Environ.*, 89, 497–509.

Brown, L.R. 1995. *Who will feed China? wake-up call for a small planet:* WW Norton & Company.

Bryan, B.A., Ye, Y., Connor, J.D. 2018. Land-use change impacts on ecosystem services value: Incorporating the scarcity effects of supply and demand dynamics. *Ecosyst. Serv.*, 32, 144–157.

Calderón-Loor, M., Hadjikakou, M., Bryan, B.A. High-resolution wall-to-wall land-cover mapping and land change assessment for Australia from 1985 to 2015. *Remote Sens. Environ.*, 252, 112148.

Chen, G., Li, X., Liu, X., Chen, Y., Liang, X., Leng, J., Xu, X., Liao, W., Wu, Q., Huang, K. 2020. Global projections of future urban land expansion under shared socioeconomic pathways. *Nat. Commun.*, 11, 1–12.

Chen, J., Jönsson, P., Tamura, M., Gu, Z., Matsushita, B., Eklundh, L. 2004. A simple method for reconstructing a high-quality NDVI time-series data set based on the Savitzky–Golay filter. *Remote Sens. Environ.*, 91, 332–344.

Clarke, K.C., Johnson, J.M. 2020. Calibrating SLEUTH with big data: projecting California's land use to 2100. *Comput. Environ. Urban Syst.*, 83, 101525.

Deng, C., Zhu, Z. 2020. Continuous subpixel monitoring of urban impervious surface using Landsat time series. *Remote Sens. Environ.*, 238, 110929.

Dong, M., Bryan, B.A., Connor, J.D., Nolan, M., Gao, L. 2015. Land use mapping error introduces strongly-localised, scale-dependent uncertainty into land use and ecosystem services modelling. *Ecosyst. Serv.*, 15, 63–74.

Elmore, A.J., Guinn, S.M., Minsley, B.J., Richardson, A.D. 2012. Landscape controls on the timing of spring, autumn, and growing season length in mid-Atlantic forests. *Global Change Biol.*, 18, 656–674.

ESA 2017. *Land cover CCI product user guide version 2:* ESA Libin, Belgium.

Fang, C., Cui, X., Li, G., Bao, C., Wang, Z., Ma, H., Sun, S., Liu, H., Luo, K., Ren, Y. 2019. Modeling regional sustainable development scenarios using the Urbanization and Eco-environment Coupler: Case study of Beijing-Tianjin-Hebei urban agglomeration, China. *Sci. Total Environ.*, 689, 820–830.

Filazzola, A., Shrestha, N., MacIvor, J.S. 2019. The contribution of constructed green infrastructure to urban biodiversity: A synthesis and meta-analysis. *J. Appl. Ecol.*, 56, 2131–2143.

Foga, S., Scaramuzza, P.L., Guo, S., Zhu, Z., Dilley Jr, R.D., Beckmann, T., Schmidt, G.L., Dwyer, J.L., Hughes, M.J., Laue, B. 2017. Cloud detection algorithm comparison and validation for operational Landsat data products. *Remote Sens. Environ.*, 194, 379–390.

Fu, Y., Li, J., Weng, Q., Zheng, Q., Le Li, Dai, S., Guo, B. 2019. Characterizing the spatial pattern of annual urban growth by using time series Landsat imagery. *Sci. Total Environ.*, 666, 274–284.

Gong, P., Li, X., Wang, J., Bai, Y., Chen, B., Hu, T., Liu, X., Xu, B., Yang, J., Zhang, W., Zhou, Y. 2020. Annual maps of global artificial impervious area (GAIA) between 1985 and 2018. *Remote Sens. Environ.*, 236.

Gong, P., Li, X., Zhang, W. 2019. 40-Year (1978–2017) human settlement changes in China reflected by impervious surfaces from satellite remote sensing. *Sci. Bull.*, 64, 756–763.

Gorelick, N., Hancher, M., Dixon, M., Ilyushchenko, S., Thau, D., Moore, R. 2017. Google Earth Engine: Planetary-scale geospatial analysis for everyone. *Remote Sens. Environ.*, 202, 18–27.

He, C., Liu, Z., Gou, S., Zhang, Q., Zhang, J., Xu, L. 2019. Detecting global urban expansion over the last three decades using a fully convolutional network. *Environ. Res. Lett.*, 14.

He, J., Yang, K., Tang, W., Lu, H., Qin, J., Chen, Y., Li, X. 2020. The first high-resolution meteorological forcing dataset for land process studies over China. *Sci. Data*, 7, 1–11.

Hopkins, F.M., Ehleringer, J.R., Bush, S.E., Duren, R.M., Miller, C.E., Lai, C.-T., Hsu, Y.-K., Carranza, V., Randerson, J.T. 2016. Mitigation of methane emissions in cities: How new measurements and partnerships can contribute to emissions reduction strategies. *Earth's Future*, 4, 408–425.

Hou, X., Feng, L., Tang, J., Song, X.-P., Liu, J., Zhang, Y., Wang, J., Xu, Y., Dai, Y., Zheng, Y. 2020. Anthropogenic transformation of Yangtze Plain freshwater lakes: patterns, drivers and impacts. *Remote Sens. Environ.*, 248, 111998.

Jin, G., Chen, K., Wang, P., Guo, B., Dong, Y., Yang, J. 2019. Trade-offs in land-use competition and sustainable land development in the North China Plain. *Technol. Forecasting Social Change*, 141, 36–46.

Jönsson, P., Cai, Z., Melaas, E., Friedl, M.A., Eklundh, L. 2018. A method for robust estimation of vegetation seasonality from Landsat and Sentinel-2 time series data. *Remote Sens.*, 10, 635.

Jun, C., Ban, Y., Li, S. 2014. Open access to Earth land-cover map. *Nature*, 514, 434.

Ke, X., van Vliet, J., Zhou, T., Verburg, P.H., Zheng, W., Liu, X. 2018. Direct and indirect loss of natural habitat due to built-up area expansion: A model-based analysis for the city of Wuhan, China. *Land Use Policy*, 74, 231–239.

Lamb, W.F., Creutzig, F., Callaghan, M.W., Minx, J.C. 2019. Learning about urban climate solutions from case studies. *Nat. Clim. Change*, 9, 279–287.

Li, G., Jiang, C., Du, J., Jia, Y., Bai, Ju %J Science of The Total Environment 2020. Spatial differentiation characteristics of internal ecological land structure in rural settlements and its response to natural and socio-economic conditions in the Central Plains, China. *Sci. Total Environ.*, 709, 135932.

Li, K., Chen, Y. 2018. A Genetic Algorithm-based urban cluster automatic threshold method by combining VIIRS DNB, NDVI, and NDBI to monitor urbanization. *Remote Sens.*, 10, 277.

Li, S., Dragicevic, S., Castro, F.A., Sester, M., Winter, S., Coltekin, A., Pettit, C., Jiang, B., Haworth, J., Stein, A. 2016. Geospatial big data handling theory and methods: A review and research challenges. *ISPRS J. Photogramm. Remote Sens.*, 115, 119–133.

Li, X., Gong, P. 2016. An "exclusion-inclusion" framework for extracting human settlements in rapidly developing regions of China from Landsat images. *Remote Sens. Environ.*, 186, 286–296.

Li, X., Gong, P., Liang, L. 2015. A 30-year (1984–2013) record of annual urban dynamics of Beijing City derived from Landsat data. *Remote Sens. Environ.*, 166, 78–90.

Li, X.C., Zhou, Y.Y., Zhu, Z.Y., Liang, L., Yu, B.L., Cao, W.T. 2018. Mapping annual urban dynamics (1985-2015) using time series of Landsat data. *Remote Sens. Environ.*, 216, 674–683.

Liu, C., Zhang, Q., Luo, H., Qi, S.H., Tao, S.Q., Xu, H.Z.Y., Yao, Y. 2019. An efficient approach to capture continuous impervious surface dynamics using spatial-temporal rules and dense Landsat time series stacks. *Remote Sens. Environ.*, 229, 114–132.

Liu, X.P., Hu, G.H., Chen, Y.M., Li, X., Xu, X.C., Li, S.Y., Pei, F.S., Wang, S.J. 2018. High-resolution multi-temporal mapping of global urban land using Landsat images based on the Google Earth Engine Platform. *Remote Sens. Environ.*, 209, 227–239.

Liu, Y., Liu, L., Zhu, A.-X., Lao, C., Hu, G., Hu, Yueming %J Land Use Policy 2020. Scenario farmland protection zoning based on production potential: A case study in China. *Land Use Policy*, 95, 104581.

National Bureau of Statistics of China., 2019a. Announcement of the 2019 grain output.

http://www.gov.cn/xinwen/2019-12/07/content_5459250.htm (accessed 3 December 2020).

National Bureau of Statistics of China., 2019b, China Statistical Yearbook. China Statistics Press, Beijing, China.

Odenweller, J.B., Johnson, K.I. 1984. Crop identification using Landsat temporal-spectral profiles. *Remote Sens. Environ.*, 14, 39–54.

Pesaresi, M., Ehrilch, D., Florczyk, A.J., Freire, S., Julea, A., Kemper, T., Soille, P., Syrris, V. 2015. GHS built-up grid, derived from Landsat, multitemporal (1975, 1990, 2000, 2014). *European Commission, Joint Research Centre, JRC Data Catalogue*.

Poursanidis, D., Chrysoulakis, N., Mitraka, Z. 2015. Landsat 8 vs. Landsat 5: A comparison based on urban and peri-urban land cover mapping. *Int. J. Appl. Earth Obs. Geoinf.*, 35, 259–269.

Schneider, A., Mertes, C.M. 2014. Expansion and growth in Chinese cities, 1978–2010. *Environ. Res. Lett.*, 9, 24008.

Shrivastava, M., Andreae, M.O., Artaxo, P., Barbosa, H.M.J., Berg, L.K., Brito, J., Ching, J., Easter, R.C., Fan, J., Fast, J.D. 2019. Urban pollution greatly enhances formation of natural aerosols over the Amazon rainforest. *Nat. Commun.*, 10, 1–12.

Song, W., Deng, X. 2015. Effects of urbanization-induced cultivated land loss on ecosystem services in the North China Plain. *Energies*, 8, 5678–5693.

Song, X.P., Sexton, J.O., Huang, C.Q., Channan, S., Townshend, J.R. 2016. Characterizing the magnitude, timing and duration of urban growth from time series of Landsat-based estimates of impervious cover. *Remote Sens. Environ.*, 175, 1–13.

Stehman, S.V., Foody, G.M. 2019. Key issues in rigorous accuracy assessment of land cover products. *Remote Sens. Environ.*, 231.

Sulla-Menashe, D., Friedl, M.A. 2018. User guide to collection 6 MODIS land cover (MCD12Q1 and MCD12C1) product. *USGS: Reston, VA, USA*, 1–18.

Tallis, H.T., Ricketts, T., Guerry, A.D., Nelson, E., Ennaanay, D., Wolny, S., Olwero, N., Vigerstol, K., Pennington, D., Mendoza, G. 2011. *InVEST 2.1 beta user's guide. the natural capital project:* Stanford.

Tang, J., Zeng, J., Zhang, Q., Zhang, R., Leng, S., Zeng, Y., Shui, W., Xu, Z., Wang, Q. 2020. Self-adapting extraction of cropland phenological transitions of rotation agroecosystems using dynamically fused NDVI images. *Int. J. Biometeorol.*, 1–11.

United Nations 2014. World urbanization prospects: The 2014 revision, highlights. department

of economic and social affairs. *Population Division, United Nations*, 32.

Vannier, C., Bierry, A., Longaretti, P.-Y., Nettier, B., Cordonnier, T., Chauvin, C., Bertrand, N., Quetier, F., Lasseur, R., Lavorel, S. 2019. Co-constructing future land-use scenarios for the Grenoble region, France. *Landscape Urban Plann.*, 190, 103614.

Wang, C., Li, J., Liu, Q., Zhong, B., Wu, S., Xia, C. 2017. Analysis of differences in phenology extracted from the enhanced vegetation index and the leaf area index. *Sensors*, 17, 1982.

Wang, J., Zhang, Q., Gou, T., Mo, J., Wang, Z., Gao, M. 2018. Spatial-temporal changes of urban areas and terrestrial carbon storage in the Three Gorges Reservoir in China. *Ecol. Indic.*, 95, 343–352.

Wang, S., Azzari, G., Lobell, D.B. 2019. Crop type mapping without field-level labels: Random forest transfer and unsupervised clustering techniques. *Remote Sens. Environ.*, 222, 303–317.

Ye, Y., Bryan, B.A., Connor, J.D., Chen, L., Qin, Z., He, M. 2018. Changes in land-use and ecosystem services in the Guangzhou-Foshan Metropolitan Area, China from 1990 to 2010: Implications for sustainability under rapid urbanization. *Ecol. Indic.*, 93, 930–941.

Yue, H., He, C., Huang, Q., Yin, D., Bryan, B.A. 2020. Stronger policy required to substantially reduce deaths from PM 2.5 pollution in China. *Nat. Commun.*, 11, 1–10.

Zeng, L., Wardlow, B.D., Xiang, D., Hu, S., Li, D. 2020. A review of vegetation phenological metrics extraction using time-series, multispectral satellite data. *Remote Sens. Environ.*, 237.

Zhang, X., Liu, L., Wu, C., Chen, X., Gao, Y., Xie, S., Zhang, B. 2020. Development of a global 30 m impervious surface map using multisource and multitemporal remote sensing datasets with the Google Earth Engine platform. *Earth Syst. Sci. Data*, 12, 1625–1648.

Zhong, C., Hu, R., Wang, M., Xue, W., He, L. 2020. The Impact of Urbanization on urban agriculture: Evidence from China. *J. Cleaner Prod.*, 276, 122686.